Self-reduction bimetallic nanoparticles on ultrathin MXene nanosheets as functional platform for pesticide sensing

Fengnian Zhao[a], Yao Yao[a], Chengmei Jiang[a], Yuzhou Shao[a], Damià Barceló[c], Yibin Ying[a,b], Jianfeng Ping[a,*]

[a] School of Biosystems Engineering and Food Science, Zhejiang University, 866 Yuhangtang Road, Hangzhou 310058, P.R. China

[b] Zhejiang A&F University, Hangzhou 311300, P.R. China

[c] ICRA-Catalan Institute for Water Research, Scientific and Technological Park of the University of Girona, Emili Grahit 101, 17003 Girona, Spain

Corresponding author: Prof. Jianfeng Ping

Email: jfping@zju.edu.cn

ABSTRACT:

Two-dimensional (2D) transition metal carbides and nitrides, named MXene, appear promising application prospects in sensor filed. Metal nanoparticles, especially bimetallic nanoparticles, are the superior nanocatalyst, which process excellent features due to the high specific surface area and synergistic catalytic capacity. Using ultrathin MXene nanosheets as the natural reducing agent and support, we prepare the shape-controlled Au-Pd bimetallic nanoparticles via a self-reduction process at room temperature in a short time, which can well enhance the catalytic performance and are benefit for the acetylcholinesterase immobilization. Based on their desired properties, we propose a disposable electrochemical biosensor for the detection of organophosphorus pesticide using the multi-dimensional nanocomposites (MXene/Au-Pd) as the functional platform. Under the optimized conditions, our fabricated biosensor exhibits a favorable linear relationship with the concentration of paraoxon from 0.1 to 1000 μg L^{-1}, with a low detection limit of 1.75 ng L^{-1}. Furthermore, the biosensor can be applied for paraoxon detection in pear and cucumber samples, providing an effective and useful avenue for the applicability of novel 2D nanomaterials in biosensing field.

Keywords**:** Multi-dimensional nanocomposites; Ultrathin MXene nanosheets; Au-Pd nanoparticles; Electrochemical biosensor; Paraoxon.

1. Introduction

With the development of living standard and science technology, a great numbers of researchers have captured great interest in environmental contaminants. As one of the major pollutants, pesticide can pose a potential threat for human and non-human species health due to the illegal usage or process [1]. Among them, organophosphorus pesticides (OPs) are one kind of compounds generally containing phosphorus element, which are mainly used for the control of plant diseases, pests, and parasitic weeds [2-4]. Although some high toxic OPs have been disabled or replaced by biodegradable chemicals, the residue problems caused by them still exist in agricultural products and environment. What's more, some OPs can be oxidized into highly toxic pesticides. For example, parathion can be gradually transformed into paraoxon in the environment [5, 6], whose toxicity can cause far greater threats for human health than the original compounds. Therefore, it is of great value to establish the rapid and on-site analysis methods for OPs and their derivatives. As a typical analysis method, the electrochemical biosensor has been widely applied for the rapid and sensitive detection of pesticides. To improve the performance of electrochemical biosensor, various nanomaterials, such as graphene and metal nanoparticles, have been adopted to heighten the sensitivity, reliability, and accuracy.

Since the successfully exfoliation of graphene in 2004 [7], novel species of two-dimensional (2D) layered nanomaterials have been discovered gradually, including hexagonal boron nitride (*h*-BN) [8, 9], transition metal dichalcogenides (TMDs) [10, 11], black phosphorus (BP) [12, 13], metal-organic frameworks (MOFs) [14, 15], metal oxides [16, 17], and so on. Among them, transition metal carbides and nitrides nanosheets, labelled as MXene, have been regarded as a promising 2D nanomaterial in various research fields [18]. MXene can be obtained by the selective etching of A element using HF-based chemical method from its raw $M_{n+1}AX_n$ (MAX), where M represents an early transition metal, A is mainly a group IIIA or IVA element, and X stands for C or N element [19]. The obtained layered MXene processes favorable conductivity, hydrophilic surface, excellent mechanical stability, and rich surface chemical groups [20], which endows its wide application in energy storage [21], electromagnetic interference shielding [22], catalysis [23], and sensor [24]. Up to now, the sensors based on layered MXene have been used for the analysis of hydrogen [25-27], biomolecules [28-30], volatile gases [31, 32], and environmental pollutants [33-38]. Due to the high toxicity and risk of HF, Ghidiu et al. [39] proposed a simple method using lithium fluoride (LiF) and hydrogen chloride solution (HCl) as the alternative reagents to prepare MXene. After the appropriate sonication and centrifugation, the ultrathin MXene nanosheets can be obtained. However, only few report [40] pay attention about the application of ultrathin MXene nanosheets in environmental pollutions.

Recently, researchers tend to prepare electrochemical sensors based on nanocomposites with different dimensions to obtain the desired analytical performance [3]. 2D nanomaterials (e.g. graphene and TMDs) have always been used as the platform for the growth of various noble metal nanoparticles [41-44]. As the superior zero-dimensional (0D) catalyst, metal nanoparticles, especially bimetallic nanoparticles, can bring the promising features due to their high specific surface area and synergistic catalytic capacity [45]. Among them, gold-palladium bimetallic nanoparticles (Au-Pd NPs) are the typical bimetallic nanoparticles. However, the growth of Au-Pd NPs usually depends on reducers, such as polyvinyl pyrrolidone [46], sodium borohydride [47, 48], and ascorbic acid [49]. Besides, harsh conditions, such as high temperature [46, 49], long time, or certain potential for electrochemical deposition [50, 51] are necessary, making the application of the bimetallic nanoparticles limited. Therefore, it is meaningful to investigate the eco-friendly self-reduction template for one-step growth of Au-Pd NPs on the surface of 2D nanosheets without extra reducing agent. At present, researchers [35, 36, 52] have successfully synthesized single metal nanoparticles (e.g. Ag or Au NPs) on the surface of MXene by a simple self-reduction method, which provides a possibility for the self-reduction of Au-Pd NPs.

In this study, bimetallic nanoparticles (Au-Pd NPs) were prepared by self-reduction on the surface of ultrathin MXene ($Ti_3C_2T_x$) nanosheets. The obtained multi-dimensional nanocomposites (MXene/Au-Pd) exhibits superior conductivity and stability, which are beneficial for the electron transfer and enzyme immobilization. By combination of disposable screen-printed electrode (SPE), we fabricated a high-performance enzymatic biosensor for the rapid detection of OPs using the MXene/Au-Pd nanocomposite-based electrochemical platform (**Figure 1**). Herein, we selected paraoxon as the model pesticide due to its high toxicity and potential conversion from other OPs. Results showed that our enzymatic biosensor is easy-prepared, environment-friendly, and high sensitive, which provides a useful way for the rapid detection of paraoxon in agricultural products.

2. Experimental

2.1. Preparation of $Ti_3C_2T_x$ nanosheets

MXene nanosheets were obtained through selectively etching the Al layers of MAX phase. Briefly, Ti_3AlC_2 powder (MAX phase) was etched in LiF and HCl solution for 24 h at the temperature of 35 °C. After the centrifugation, the obtained mixture was washed with deionized water repeatedly, until the pH was closed to 7.0. Later, 1.0 g of the obtained material was dispersed into 100 mL of water with the sonication for 1 h. The stable $Ti_3C_2T_x$ nanosheets suspension was collected after the centrifugation (3500 rpm) for 1 h. Finally, MXene suspension with a concentration of 5.4 mg mL^{-1} was obtained.

2.2. *Fabrication of enzymatic biosensor*

Before the modification, the SPE was sonicated in deionized water for 2 min. After that, 10 μL of MXene suspension (diluted with deionized water into 1.0 mg mL^{-1} before use) was drop-cast on the electrode surface. Then, the MXene modified SPE (SPE/MXene) was dipped in the mixture of $HAuCl_4$ and $PdCl_2$ to prepare Au-Pd NPs on the surface of MXene via a self-reduction method (SPE/MXene/Au-Pd). Then, the cross-linking agent (0.25% GA, 10 μL) was coated on the surface of MXene/Au-Pd nanocomposites (SPE/MXene/Au-Pd/GA). After that, 10 μL of AChE (0.2 U μL^{-1}) in 2.0% BSA (1:1) was immobilized onto electrode surface (SPE/MXene/Au-Pd/GA/AChE) and dried at 35 ºC in the oven for 30 min.

2.3. *Inhibition Measurements*

Paraoxon is deemed as the inhibitor of AChE, which can lessen the output of corresponding hydrolysis product (thiocholine, TCh), consequently causing the weaker oxidation current. In actual testing, the inhibition rate (I, %) of the AChE-based biosensor usually has the linear correlation with the logarithm of paraoxon concentration ($\lg C$), which can be recorded as $I = a\lg C + b$. The typical current-time curve can be employed to test the current response of the prepared SPE/MXene/Au-Pd/GA/AChE biosensor. The inhibition rate of paraoxon was calculated as the formula $I = (I_0 – I_1) / I_0 \times 100\%$, where I_0 and I_1 represent the current response before and after the inhibition of paraoxon, respectively.

3. Results and discussion

3.1. Characterization of ultrathin $Ti_3C_2T_x$ nanosheets

The morphology and chemical structure of the MXene nanosheets was studied by SEM, TEM, and AFM. As shown in **Figure 2a-c**, the obtained nanomaterials after LiF-HCl treatment appear typical sheet-like structure with horizontal dimensions of 457 ± 86 nm. The thickness of nanosheets is 1.5 ± 0.3 nm, indicating the successful LiF-HCl induced delamination. In order to further evaluate the etching status, we compared the XRD pattern of the prepared nanosheets with that of origin MAX. **Figure 2d** shows that the non-basal plane peak of Ti_3AlC_2 (the most notable peak at $2\theta \approx 39°$) [19] disappears after the treatment, proving that the Al layers are totally etched away. In addition, some diffraction peaks of $Ti_3C_2T_x$, such as (002), (004), and (0010) peaks, tend to be broadened, weak, and shift to lower angles. All of these demonstrate that the ultrathin $Ti_3C_2T_x$ nanosheets are prepared successfully.

3.2. Characterization of SPE/MXene/Au-Pd

As shown in **Figure S1a**, the surface of SPE was covered with MXene nanosheets, which forms into the uniform and rough film. Then, the MXene nanosheets-based SPE (SPE/MXene) was soaked into Au^{3+}-Pd^{2+} mixture to grow bimetallic nanoparticles. In order to obtain the favorable Au-Pd NPs, we optimized the growth time and the concentration ratio of Au^{3+}-Pd^{2+} mixture. Firstly, we set different immersion time from 0 s to 10 min in 5 mM Au^{3+}-Pd^{2+} mixture (the concentration ratio of Au^{3+} to Pd^{2+} is 1:1). As illustrated in **Figure S1**, the nanoparticles can grow on the surface of MXene nanosheets immediately, and the size of nanoparticles is about 30~80 nm only after a self-reduction reaction time of 5 s (**Figure S1b**). As time goes on, the density and size of nanoparticles on MXene film become greater. After 5 min, the nanoparticles appear homogeneous distribution on the surface of MXene nanosheets (**Figure S1g**). The energy dispersive spectrometer (EDS) mapping images (the growth time is 5 min) shows the distribution of Au, Pd, Ti, and C elements on the surface of the electrode (**Figure S1i**), indicating the successful in-situ growth of Au-Pd NPs on MXene nanosheets. To make it clear, differential pulse voltammetry (DPV) was used to compare the current response of electrodes in different growth time. From **Figure 3a**, the current response gradually increases until 5 min. After that, the current response decreases, which is probably due to the overcrowded NPs influence the electron transfer kinetics. In view of the NPs morphology and DPV response, we chose 5 min as the optimized growth time for Au-Pd NPs.

Then, we optimized different concentration ratios of Au^{3+}-Pd^{2+} precursor mixture. As the increasing concentration ratio of Pd^{2+} in the precursor mixture, the bimetallic nanoparticles become big and rough (**Figure S2a-d**), and the atomic ratio of Pd element in Au-Pd NPs goes higher (**Figure S2f**). Compared with the pure Pd^{2+} solution (**Figure S2e**), the introduction of Au^{3+} in the precursor mixture can efficiently promote the growth of Pd NPs on MXene nanosheets, probably due to the lower reduction potential of Au^{3+} than that of Pd^{2+}. When the concentration ratio of Au^{3+} to Pd^{2+} is 1:2, the DPV response gets the maximum (**Figure 3b**). Given all that, we chose the concentration ratio of 1:2 for Au^{3+}-Pd^{2+} precursor. The SEM and EDS images in **Figure 4a, c** display the morphology and elemental mapping analysis of bimetallic nanoparticles on the surface of MXene nanosheets at high magnification under the optimized conditions, indicating the successful preparation of Au-Pd NPs on the surface of MXene nanosheets. Besides, we compared the XRD patterns of MXene before/after the growth of Au-Pd NPs. From **Figure 4b**, the main peaks of MXene/Au-Pd nanocomposites are consistent with that of MXene, together with the (111) planes of Au and Pd ($2\theta \approx 40°$), as well as the (200) plane of Au (2θ≈45°) in the JCPD card, which further verifies the formation of Au-Pd NPs.

3.3. *Electrochemical response of enzymatic biosensor*

Electrochemical impedance spectroscopy (EIS) was used to study the electron transfer properties of the different modified SPEs. From **Figure 5a**, all of the EIS curves appear a typical semi-circle or straight line in the high/low frequency scope. It is clear that SPE/MXene (pink line) has very small semicircle diameter of EIS curve compared with bare SPE (gray line), which is due to the excellent conductivity and favorable electron transfer kinetics of this sheet-like nanomaterials. After different modifications, the EIS curves display different semicircle diameters. When Au-Pd NPs were generated on MXene nanosheets, the SPE/MXene/Au-Pd (purple line) has a relatively large electron-transfer resistance. A report [53] states that metal NPs can boost the removal of surface functional groups and reduction of the early transition metal elements of MXene. It might be the reason why the self-reduction of Au-Pd NPs somewhat affects the original properties of MXene nanosheets. After modified AChE, the semicircle diameter of the biosensor (SPE/MXene/Au-Pd/GA/AChE) has a significant increase, indicating the effective immobilization of enzyme. **Figure S3** displays the CV response of the different modified SPEs in 0.1 M KCl solution containing 5.0 mM $K_3[Fe(CN)_6]$. After modified with MXene/Au-Pd nanocomposites, the reduction peak is obviously higher than that of bare SPE, indicating the excellent electrochemical conductivity of the prepared nanocomposites. Interestingly, the Au-Pd metallic nanoparticles can well ameliorate the CV curve of SPE/MXene, which could not form the typical oxidation-reduction couples in 5.0 mM $K_3[Fe(CN)_6]$ solution. After immobilized AChE, the CV response become weaker. All of above match with the EIS measurement results (**Figure 5a**).

After that, we studied the DPV response of the obtained biosensor (SPE/MXene/Au-Pd/GA/AChE) in the absence/presence of ATCh. From **Figure S4**, the prepared biosensor has an obvious oxidation peak around 0.45 V, which is owning to the hydrolysis of ATCh. To verify the better electrochemical performance of our biosensor after the modification of Au-Pd NPs, we tested the electrochemical response of the different electrodes towards ATCh via an amperometric titration under 0.45 V. From **Figure 5b**, the current response of our enzymatic biosensor (green line) is much higher than that of other enzyme-free electrodes with the addition of ATCh, indicating the high electrocatalytic activity of the fabricated biosensor. Besides, the bimetallic nanoparticles modified electrode (pink line) has the same current response trend as AChE-modified biosensor (green line), verifying the internal catalytic function of Au-Pd NPs. Compared with none-bimetallic nanoparticles modified enzymatic biosensor (SPE/MXene/GA/AChE, purple line), our biosensor appears the higher current signal, indicating the favorable synergistic catalysis effect of Au-Pd NPs and AChE.

3.4. Paraoxon detection

As described above, paraoxon can inhibit the activity of AChE, consequently causing the weaker electrochemical signal. Therefore, the concentration of paraoxon can be calculated through the inhibition rate of AChE. Here, the amperometric method was adopted for the electrochemical detection of pesticide. Before the experiment, the inhibition time and substrate (ATCh) concentration of the prepared biosensor were optimized by comparing the inhibition rate of AChE in the presence of paraoxon (20 μg L^{-1}). As shown in **Figure S5a**, the inhibition rate tends to increase with the increase of inhibition time. After 10 min, the inhibition rate reaches saturation. Then, the concentration of ATCh is optimized with the inhibition time of 10 min. When the concentration of ATCh is 1.0 mM, the maximum inhibition rate appears (**Figure S4b**). From the above, the optimized inhibition time and substrate concentration are chosen as 10 min and 1.0 mM, respectively.

Under the optimized conditions, the amperometric response declined obviously with the increase of the concentration of paraoxon (**Figure 6a**). When paraoxon concentration is from 0.1 to 1000 μg L^{-1} (*i.e.*, 0.36–3634 nM in mol representation), the corresponding inhibition rate has a linear relation with the logarithm of its concentration. By fitting, the linear equation of paraoxon is $I = 23\lg C + 20$ ($R^2 = 0.9837$), where I represents the inhibition rate and C represents the paraoxon concentration. The linear equation was also analyzed by linear least-square regression with the relevant results reported with confidence interval for 95% probability (**Figure 6b**). Based on the triple signal-to-noise ratio, the detection limit is calculated to be 1.75 ng L^{-1} (*i.e.*, 6.36 pM in mol representation). The DPV responses of the fabricated biosensor for paraoxon have the same decreasing tendency, which is recorded in **Figure S6**. Compared with the other MXene-based biosensors, our proposed biosensor has the comparable analytical performance for pesticide detection (**Table S1**).

3.5. *Selectivity, interference, and stability study*

To investigate the selectivity of the fabricated biosensor, the inhibition rates of other three OPs, including ethyl-paraoxon, ediphenphos, and fenitrothion are compared with that of paraoxon (20 μg L^{-1}). From **Figure S7a**, the inhibition rate for ethyl-paraoxon, ediphenphos, and fenitrothion are 51.7%, 23.2%, and 17.6%, respectively, which are all lower than that of paraoxon, implying the favorable selectivity of our biosensor towards the model pesticide.

The interference study was assessed by comparing the amperometric signal with/without the addition of some possible interferents. The corresponding results are present in **Figure S7b**. For 5 mM of metal ions (i.e. K^+, Ca^{2+}, Zn^{2+}, and Mg^{2+}), there is a slight current change, which means that the usual electroactive species cannot cause the obvious interference for the fabricated biosensor. Phenol has been extensively used as the pesticide intermediate in the process of synthesis and has the homologous structure of OPs. Therefore, we investigated the interference of 100 mM of phenol for the prepared biosensor. It is clear that the interference of phenol is negligible, indicating the satisfying selectivity for target pesticide. To make the real agricultural product samples analysis possible, we explored the potential sample interferences, such as ascorbic acid and glucose. Results show that the only ascorbic acid (100 mM) can generate obvious current increase. This is due to the change of pH value induced by ascorbic acid, which is distinctly different from the optimized condition for the prepared biosensor.

In addition, we discussed the interference of the dissolved organic matter (DOM) in agriculture runoff. Herein, the local lake water was selected as the tested sample. The collected lake water was filtrated with 0.45 μm filter membrane as the prepared DOM solution, of which the concentration of the dissolved organic carbon (DOC) was 8.04 mg L^{-1}. Then, the DOM solution (2 mL) was diluted with 0.01 M PBS into 10 mL and tested the amperometric signal in the presence of ATCh. Results show that the interference of DOM is negligible (**Figure S7b**), indicating the favorable anti-interference property of our prepared biosensor.

In this study, the fabricated biosensor was sealed and stored in the refrigerator at 4 °C when not in use. The storage stability of the biosensor was investigated the amperometric response of the biosensor in 0.01 M PBS containing 1.0 mM ATCh. Results indicate that the biosensor can maintain 95% of the original response after seven days, illustrating the satisfying stability.

3.6. *Analysis of real samples*

Recovery experiments are used to evaluate the applicability of the fabricated biosensor in agricultural products. Pears and cucumbers were selected as the real samples. Three spiking levels (5, 10, and 20 μg L^{-1}) in blank samples were set in this experiment. To reduce the interferences in samples, 25 mg PSA and C_{18} were employed as the cleaning agents. The detailed pretreatment steps followed our recent reports [6]. As shown in **Table S2**, the recoveries of paraoxon in pear and cucumber samples are from 87.93% to 111.02%, with the relative standard deviations (RSDs) from 1.08% to 6.37% (n=3). The above results conformably reveal that our fabricated biosensor is of acceptable reliability and accuracy, making the practical analysis of paraoxon in agricultural products come true.

4. Conclusions

In summary, an AChE-based pesticide biosensor was fabricated for the electrochemical determination of OPs using MXene/Au-Pd nanocomposites as the functional platform. Here, Au-Pd bimetallic nanoparticles were synthesized through a self-reduction reaction on the surface of ultrathin MXene nanosheets, where MXene nanosheets act as the natural reductants and supports. Results indicate that the Au-Pd NPs are not only shape-controlled and easy-prepared, but also of desired catalytic activity, which can cooperate with AChE to effectively catalyze the hydrolysis of ATCh. Besides, the MXene/Au-Pd nanocomposites possess superior conductivity and large specific surface area, which plays an important part for electron transfer and AChE immobilization. Using paraoxon as the model pesticide, the established biosensor shows wide linear range, low detection limit, favorable sensitivity, and real sample applicability, which can broaden the application of ultrathin MXene nanosheets for environmental contaminants analysis.

Acknowledgements

This work was supported by the National Key Research and Development Program of China (No. 2017YFF0211300).

References

[1] F.P. Carvalho, Pesticides, environment, and food safety, Food Energy Secur. 6 (2017) 48-60.

[2] N. Kaur, N. Prabhakar, Current scenario in organophosphates detection using electrochemical biosensors, TrAC Trends Anal. Chem. 92 (2017) 62-85.

[3] F. Zhao, J. Wu, Y. Ying, Y. She, J. Wang, J. Ping, Carbon nanomaterial-enabled pesticide biosensors: Design strategy, biosensing mechanism, and practical application, TrAC Trends Anal. Chem. 106 (2018) 62-83.

[4] W. Tang, J. Yang, F. Wang, J. Wang, Z. Li, Thiocholine-triggered reaction in personal glucose meters for portable quantitative detection of organophosphorus pesticide, Anal. Chim. Acta 1060 (2019) 97-102.

[5] J.V. Kumar, R. Karthik, S.M. Chen, K. Natarajan, C. Karuppiah, C.C. Yang, V. Muthuraj, 3D flower-like gadolinium molybdate catalyst for efficient detection and degradation of organophosphate pesticide (fenitrothion), ACS Appl. Mater. Interfaces 10 (2018) 15652-15664.

[6] F. Zhao, Y. Yao, X. Li, L. Lan, C. Jiang, J. Ping, Metallic transition metal dichalcogenide nanosheets as an effective and biocompatible transducer for electrochemical detection of pesticide, Anal. Chem. 90 (2018) 11658-11664.

[7] K. S. Novoselov, A. K. Geim, S. V. Morozov, D. Jiang, Y. Zhang, S. V. Dubonos, I. V. Grigorieva, A.A. Firsov, Electric field effect in atomically thin carbon films, Nature 306 (2004) 666-669.

[8] M.Y. Musa, M. Renuka, X. Lin, R. Li, H. Wang, E. Li, B. Zhang, H. Chen, Confined transverse electric phonon polaritons in hexagonal boron nitrides, 2D Mater. 5 (2018) 015018.

[9] L. Liu, J. Park, D.A. Siegel, K.F. McCarty, K.W. Clark, W. Deng, L. Basile, J.C. Idrobo, A.P. Li, G. Gu, Heteroepitaxial growth of two-dimensional hexagonal boron nitride templated by graphene edges, Science 343 (2014) 163-167.

[10] B.L. Li, J.P. Wang, H.L. Zou, S. Garaj, C.T. Lim, J.P. Xie, N.B. Li, D.T. Leong, Low-dimensional transition metal dichalcogenide nanostructures based sensors, Adv. Funct. Mater. 26 (2016) 7034-7056.

[11] J.F. Ping, Z.X. Fan, M. Sindoro, Y.B. Ying, H. Zhang, Recent advances in sensing applications of two-dimensional transition metal dichalcogenide nanosheets and their composites, Adv. Funct. Mater. 27 (2017) 1605817.

[12] P.F. Chen, N. Li, X.Z. Chen, W.J. Ong, X.J. Zhao, The rising star of 2D black phosphorus beyond graphene: synthesis, properties and electronic applications, 2D Mater. 5 (2018) 014002.

[13] M. Engel, M. Steiner, P. Avouris, Black phosphorus photodetector for multispectral, high-resolution imaging, Nano Lett. 14 (2014) 6414-6417.

[14] M. Zhao, Y. Wang, Q. Ma, Y. Huang, X. Zhang, J. Ping, Z. Zhang, Q. Lu, Y. Yu, H. Xu, Y. Zhao, H. Zhang, Ultrathin 2D metal-organic framework nanosheets, Adv. Mater. 27 (2015) 7372-7378.

[15] M.T. Zhao, Y. Huang, Y.W. Peng, Z.Q. Huang, Q.L. Ma, H. Zhang, Two-dimensional

metal-organic framework nanosheets: synthesis and applications, Chem. Soc. Rev. 47 (2018) 6267-6295.

[16] A. Zavabeti, J.Z. Ou, B.J. Carey, N. Syed, R. Orrell-Trigg, E.L.H. Mayes, C.L. Xu, O. Kavehei, A.P. O'Mullane, R.B. Kaner, K. Kalantar-Zadeh, T. Daeneke, A liquid metal reaction environment for the room-temperature synthesis of atomically thin metal oxides, Science 358 (2017) 332-335.

[17] Z.M. Hu, X. Xiao, H.Y. Jin, T.Q. Li, M. Chen, Z. Liang, Z.F. Guo, J. Li, J. Wan, L. Huang, Y.R. Zhang, G. Feng, J. Zhou, Rapid mass production of two-dimensional metal oxides and hydroxides via the molten salts method, Nat. Commun. 8 (2017) 15630.

[18] M. Naguib, V.N. Mochalin, M.W. Barsoum, Y. Gogotsi, 25th anniversary article: MXenes: A new family of two-dimensional materials, Adv. Mater. 26 (2014) 992-1005.

[19] M. Naguib, M. Kurtoglu, V. Presser, J. Lu, J.J. Niu, M. Heon, L. Hultman, Y. Gogotsi, M.W. Barsoum, Two-dimensional nanocrystals produced by exfoliation of Ti_3AlC_2, Adv. Mater. 23 (2011) 4248-4253.

[20] L.Y. Xiu, Z.Y. Wang, M.Z. Yu, X.H. Wu, J.S. Qiu, Aggregation-resistant 3D MXene-based architecture as efficient bifunctional electrocatalyst for overall water splitting, ACS Nano 12 (2018) 8017-8028.

[21] X. Zhang, Z.H. Zhang, Z. Zhou, MXene-based materials for electrochemical energy storage, J. Energ. Chem. 27 (2018) 73-85.

[22] R.H. Sun, H.B. Zhang, J. Liu, X. Xie, R. Yang, Y. Li, S. Hong, Z.Z. Yu, Highly conductive transition metal carbide/carbonitride(MXene)@polystyrene nanocomposites fabricated by electrostatic assembly for highly efficient electromagnetic interference shielding, Adv. Funct.

Mater. 27 (2017) 1702807.

[23] J.Y. Diao, M.M. Hu, Z. Lian, Z.J. Li, H. Zhang, F. Huang, B. Li, X.H. Wang, D.S. Su, H.Y. Liu, $Ti_3C_2T_x$ MXene catalyzed ethylbenzene dehydrogenation: Active sites and mechanism exploration from both experimental and theoretical aspects, ACS Catal. 8 (2018) 10051-10057.

[24] A. Sinha, Dhanjai, H.M. Zhao, Y.J. Huang, X.B. Lu, J.P. Chen, R. Jain, MXene: An emerging material for sensing and biosensing, TrAC Trends Anal. Chem. 105 (2018) 424-435.

[25] L. Lorencova, T. Bertok, E. Dosekova, A. Holazova, D. Paprckova, A. Vikartovska, V. Sasinkova, J. Filip, P. Kasak, M. Jerigova, D. Velic, K.A. Mahmoud, J. Tkac, Electrochemical performance of $Ti_3C_2T_x$ MXene in aqueous media: towards ultrasensitive H_2O_2 sensing, Electrochim. Acta 235 (2017) 471-479.

[26] J.S. Zheng, J.L. Diao, Y.Z. Jin, A.L. Ding, B. Wang, L.Z. Wu, B. Weng, J.C. Chen, An Inkjet printed Ti_3C_2-GO electrode for the electrochemical sensing of hydrogen peroxide, J. Electrochem. Soc. 165 (2018) B227-B231.

[27] L. Lorencova, T. Bertok, J. Filip, M. Jerigova, D. Velic, P. Kasak, K.A. Mahmoud, J. Tkac, Highly stable $Ti_3C_2T_x$ (MXene)/Pt nanoparticles-modified glassy carbon electrode for H_2O_2 and small molecules sensing applications, Sens. Actuators B Chem. 263 (2018) 360-368.

[28] S. Kumar, Y. Lei, N.H. Alshareef, M.A. Quevedo-Lopez, K.N. Salama, Biofunctionalized two-dimensional Ti_3C_2 MXenes for ultrasensitive detection of cancer biomarker, Biosens. Bioelectron. 121 (2018) 243-249.

[29] J. Zheng, B. Wang, A. Ding, B. Weng, J. Chen, Synthesis of MXene/DNA/Pd/Pt nanocomposite for sensitive detection of dopamine, J. Electroanal. Chem. 816 (2018) 189-194.

[30] Y.F. Fang, X.C. Yang, T. Chen, G.F. Xu, M.L. Liu, J.Q. Liu, Y.H. Xu, Two-dimensional

titanium carbide (MXene)-based solid-state electrochemiluminescent sensor for label-free single-nucleotide mismatch discrimination in human urine, Sens. Actuators B Chem. 263 (2018) 400-407.

[31] E. Lee, A.V. Mohammadi, B.C. Prorok, Y.S. Yoon, M. Beidaghi, D.J. Kim, Room temperature gas sensing of two-dimensional titanium carbide (MXene), ACS Appl. Mater. Interfaces 9 (2017) 37184-37190.

[32] X. Tang, A.J. Du, L.Z. Kou, Gas sensing and capturing based on two-dimensional layered materials: Overview from theoretical perspective, WIREs. Comput. Mol. Sci. 8 (2018) e1361.

[33] L.X. Wu, X.B. Lu, Dhanjai, Z.S. Wu, Y.F. Dong, X.H. Wang, S.H. Zheng, J.P. Chen, 2D transition metal carbide MXene as a robust biosensing platform for enzyme immobilization and ultrasensitive detection of phenol, Biosens. Bioelectron. 107 (2018) 69-75.

[34] L. Zhou, X. Zhang, L. Ma, J. Gao, Y. Jiang, Acetylcholinesterase/chitosan-transition metal carbides nanocomposites-based biosensor for the organophosphate pesticides detection, Biochem. Eng. J. 128 (2017) 243-249.

[35] Y.J. Jiang, X.N. Zhang, L.J. Pei, S. Yue, L. Ma, L.Y. Zhou, Z.H. Huang, Y. He, J. Gao, Silver nanoparticles modified two-dimensional transition metal carbides as nanocarriers to fabricate acetycholinesterase-based electrochemical biosensor, Chem. Eng. J. 339 (2018) 547-556.

[36] D. Song, X. Jiang, Y. Li, X. Lu, S. Luan, Y. Wang, Y. Li, F. Gao, Metal-organic frameworks-derived MnO_2/Mn_3O_4 microcuboids with hierarchically ordered nanosheets and $Ti_3C_2T_x$ MXene/Au NPs composites for electrochemical pesticide detection, J. Hazard. Mater. 373 (2019) 367-376.

[37] H. Xie, P. Li, J. Shao, H. Huang, Y. Chen, Z. Jiang, P.K. Chu, X.F. Yu, Electrostatic self-assembly of $Ti_3C_2T_x$ MXene and gold nanorods as an efficient surface-enhanced Raman scattering platform for reliable and high-sensitivity determination of organic pollutants, ACS Sens. (2019). DOI: 10.1021/acssensors.9b00778.

[38] D. Wu, M. Wu, J. Yang, H. Zhang, K. Xie, C.T. Lin, A. Yu, J. Yu, L. Fu, Delaminated $Ti_3C_2T_x$ (MXene) for electrochemical carbendazim sensing, Mater. Lett. 236 (2019) 412-415.

[39] M. Ghidiu, M.R. Lukatskaya, M.Q. Zhao, Y. Gogotsi, M.W. Barsoum, Conductive two-dimensional titanium carbide 'clay' with high volumetric capacitance, Nature 516 (2014) 78-81.

[40] B. Yu, B. Tawiah, L.Q. Wang, A.C. Yin Yuen, Z.C. Zhang, L.L. Shen, B. Lin, B. Fei, W. Yang, A. Li, S.E. Zhu, E.Z. Hu, H.D. Lu, G.H. Yeoh, Interface decoration of exfoliated MXene ultra-thin nanosheets for fire and smoke suppressions of thermoplastic polyurethane elastomer, J. Hazard. Mater. 374 (2019) 110-119.

[41] O. Parlak, A. Incel, L. Uzun, A.P.F. Turner, A. Tiwari, Structuring Au nanoparticles on two-dimensional MoS_2 nanosheets for electrochemical glucose biosensors, Biosens. Bioelectron. 89 (2017) 545-550.

[42] J.J. Wu, Y.L. Lu, Z.Q. Wu, S. Li, Q. Zhang, Z.T. Chen, J. Jiang, S.S. Lin, L. Zhu, C.D. Li, Q.J. Liu, Two-dimensional molybdenum disulfide (MoS_2) with gold nanoparticles for biosensing of explosives by optical spectroscopy, Sens. Actuators B Chem. 261 (2018) 279-287.

[43] Y. Zhang, Z. Xia, Q.Z. Li, G.F. Gui, G.Y. Zhao, L.L. Lin, Surface controlled electrochemical sensing of chlorpyrifos in pinellia ternate based on a one step synthesis of palladium-reduced graphene nanocomposites, J. Electrochem. Soc. 164 (2017) B48-B53.

[44] M. Guler, V. Turkoglu, Z. Basi, Determination of malation, methidathion, and chlorpyrifos ethyl pesticides using acetylcholinesterase biosensor based on Nafion/Ag@rGO-NH_2 nanocomposites, Electrochim. Acta 240 (2017) 129-135.

[45] L. Zhang, Z.X. Xie, J.L. Gong, Shape-controlled synthesis of Au-Pd bimetallic nanocrystals for catalytic applications, Chem. Soc. Rev. 45 (2016) 3916-3934.

[46] X. Lu, L. Tao, D.D. Song, Y. Li, F.M. Gao, Bimetallic Pd@Au nanorods based ultrasensitive acetylcholinesterase biosensor for determination of organophosphate pesticides, Sens. Actuators B Chem. 255 (2018) 2575-2581.

[47] M. Wen, K. Mori, Y. Kuwahara, H. Yamashita, Plasmonic Au@Pd nanoparticles supported on a basic metal-organic framework: Synergic boosting of H_2 production from formic acid, ACS Energy Lett. 2 (2017) 1-7.

[48] W. Yan, Z.H. Tang, L.K. Wang, Q.N. Wang, H.Y. Yang, S.W. Chen, PdAu alloyed clusters supported by carbon nanosheets as efficient electrocatalysts for oxygen reduction, Int. J. Hydrogen Energ. 42 (2017) 218-227.

[49] X.Y. Li, X.Z. Du, Molybdenum disulfide nanosheets supported Au-Pd bimetallic nanoparticles for non-enzymatic electrochemical sensing of hydrogen peroxide and glucose, Sens. Actuators B Chem. 239 (2017) 536-543.

[50] H.J. Zhan, J. Li, Z.M. Liu, Y.Y. Zheng, Y.F. Jing, A highly sensitive electrochemical OP biosensor based on electrodeposition of Au-Pd bimetallic nanoparticles onto a functionalized graphene modified glassy carbon electrode, Anal. Methods 7 (2015) 3903-3911.

[51] S.C. Barman, M.F. Hossain, H. Yoon, J.Y. Park, Trimetallic Pd@Au@Pt nanocomposites platform on -COOH terminated reduced graphene oxide for highly sensitive CEA and PSA

biomarkers detection, Biosens. Bioelectron. 100 (2018) 16-22.

[52] K.K. Li, T.F. Jiao, R.R. Xing, G.D. Zou, J.X. Zhou, L.X. Zhang, Q.M. Peng, Fabrication of tunable hierarchical MXene@AuNPs nanocomposites constructed by self-reduction reactions with enhanced catalytic performances, Sci. China Mater. 61 (2018) 728-736.

[53] Z. Li, L. Yu, C. Milligan, T. Ma, L. Zhou, Y.R. Cui, Z.Y. Qi, N. Libretto, B. Xu, J.W. Luo, E.Z. Shi, Z.W. Wu, H.L. Xin, W.N. Delgass, J.T. Miller, Y. Wu, Two-dimensional transition metal carbides as supports for tuning the chemistry of catalytic nanoparticles, Nat. Commun. 9 (2018) 5258.

Figure captions

Figure 1. Schematic diagram of the preparation of MXene nanosheets and the enzyme-based pesticide biosensor using MXene/Au-Pd nanocomposites obtaining from a self-reduction strategy.

Figure 2. (a) SEM, (b) TEM, and (c) AFM images of the MXene nanosheets. Inset of b is the horizontal dimension distribution, and inset of c is the highlight profile of the selected area of MXene nanosheets. (d) XRD analysis of the MAX (Ti_3AlC_2) and MXene ($Ti_3C_2T_x$ nanosheets).

Figure 3. DPV response of SPE/MXene/Au-Pd with (a) different growth time of Au-Pd NPs and (b) different concentration ratios of Au^{3+} to Pd^{2+} in 0.1 M KCl solution containing 5.0 mM $K_3[Fe(CN)_6]$.

Figure 4. (a) SEM for SPE/MXene/Au-Pd. (b) XRD analysis of the MXene before/after the growth of Au-Pd NPs. (c) SEM image and corresponding elemental mapping analysis of Au, Pd, Ti, and C elements of the selected area for SPE/MXene/Au-Pd.

Figure 5. (a) EIS of the different SPEs in 0.1 M KCl solution containing 5.0 mM $K_3[Fe(CN)_6]$. The frequency ranges from 10 kHz to 0.1 Hz, and AC amplitude is 10 mV. (b) Amperometric response of the different SPEs with the addition of ATCh in 0.01 M PBS (pH 7.4) at 0.45 V. Each arrow represents the addition point of 0.5 mM ATCh.

Figure 6. (a) Amperometric response of SPE/MXene/Au-Pd/GA/AChE biosensor in 0.01 M PBS (pH 7.4) containing 1.0 mM ATCh after inhibition with different concentrations of paraoxon under the optimized conditions. (b) The corresponding calibration curve and its 95% confidence intervals of inhibition rate versus paraoxon concentration.

456 **Figure 1.**

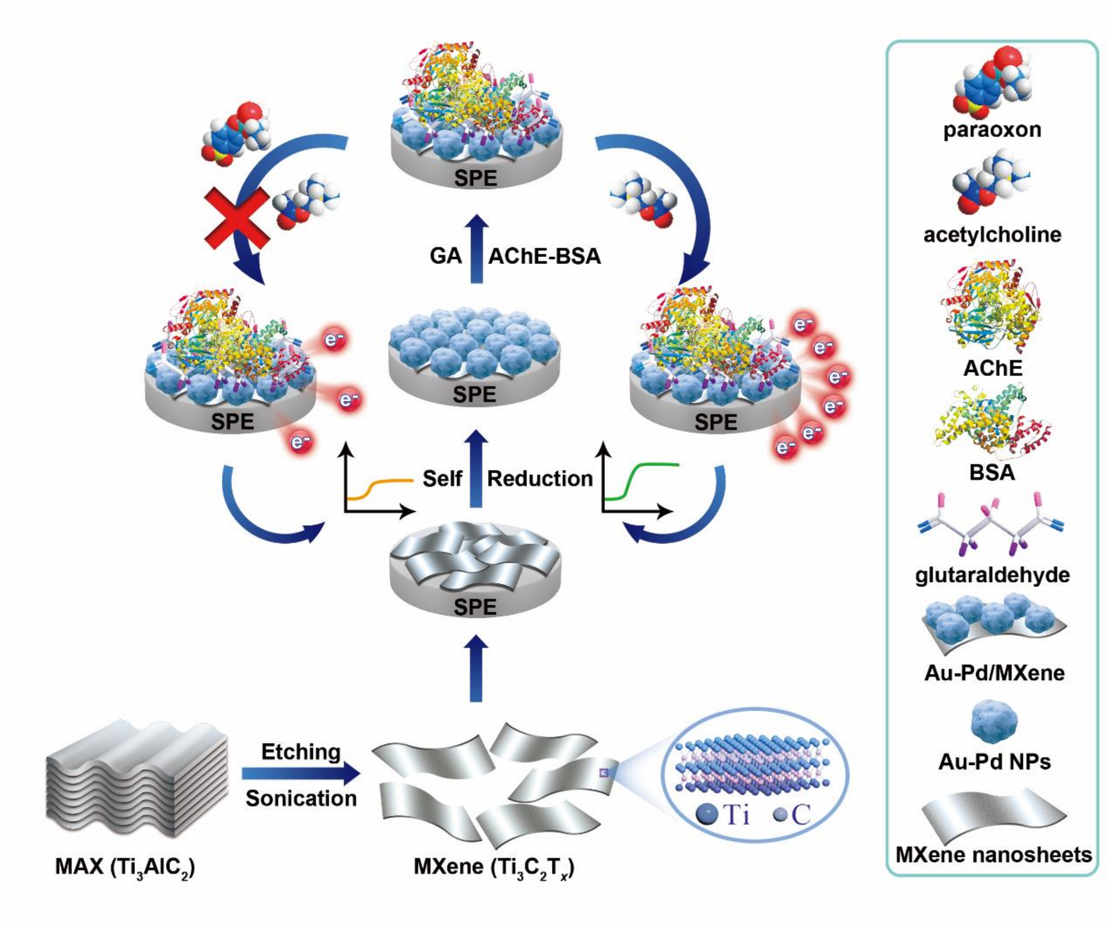

457

Figure 2.

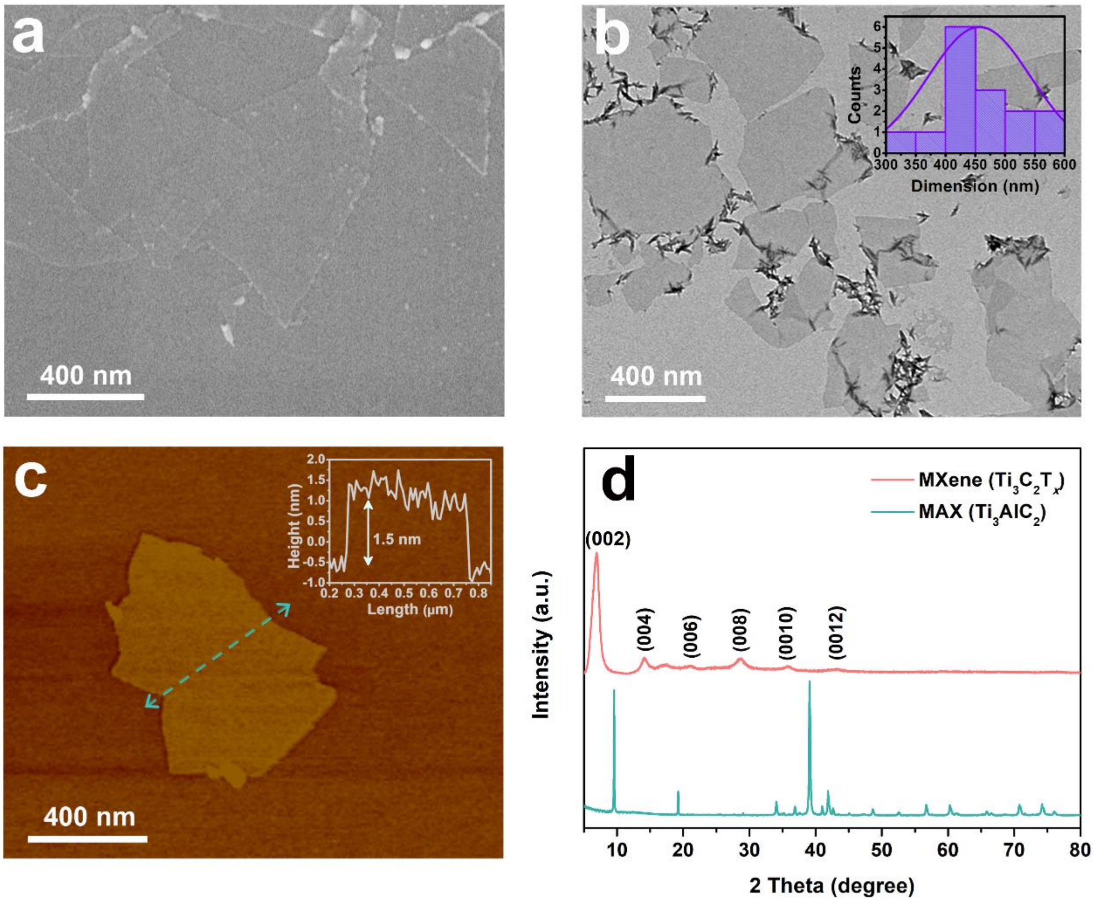
a
400 nm
b
Counts
0
1
2
3
4
5
6
300
350
400
450
500
550
600
Dimension (nm)
400 nm
c
Height (nm)
2.0
1.5
1.0
0.5
0.0
-0.5
-1.0
0.2
0.3
0.4
0.5
0.6
0.7
0.8
Length (μm)
1.5 nm
400 nm
d
MXene ($Ti_3C_2T_x$)
MAX (Ti_3AlC_2)
(002)
(004)
(006)
(008)
(0010)
(0012)
Intensity (a.u.)
10
20
30
40
50
60
70
80
2 Theta (degree)

Figure 3.

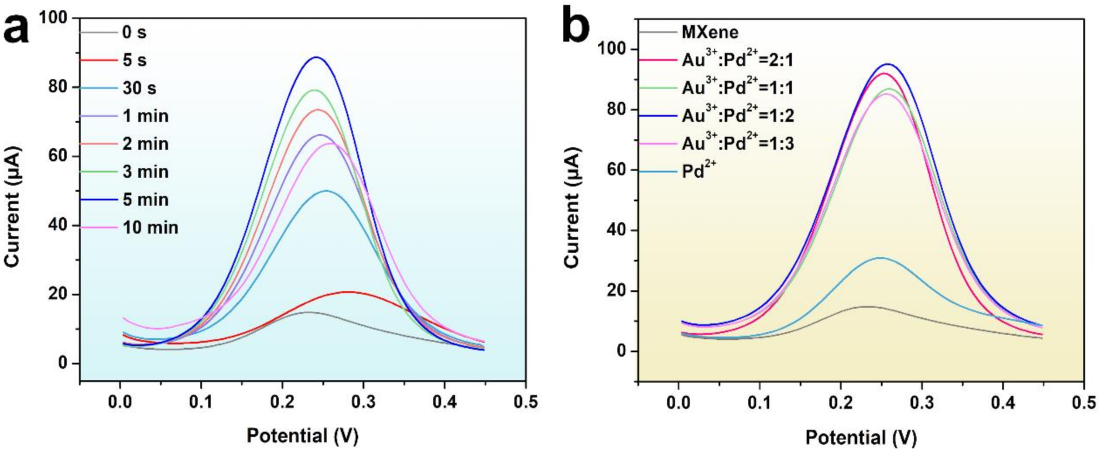
a
Current (μA)
Potential (V)
0 s
5 s
30 s
1 min
2 min
3 min
5 min
10 min
0
20
40
60
80
100
0.0
0.1
0.2
0.3
0.4
0.5
b
Current (μA)
Potential (V)
MXene
Au^{3+}:Pd^{2+}=2:1
Au^{3+}:Pd^{2+}=1:1
Au^{3+}:Pd^{2+}=1:2
Au^{3+}:Pd^{2+}=1:3
Pd^{2+}
0
20
40
60
80
100
0.0
0.1
0.2
0.3
0.4
0.5

Figure 4.

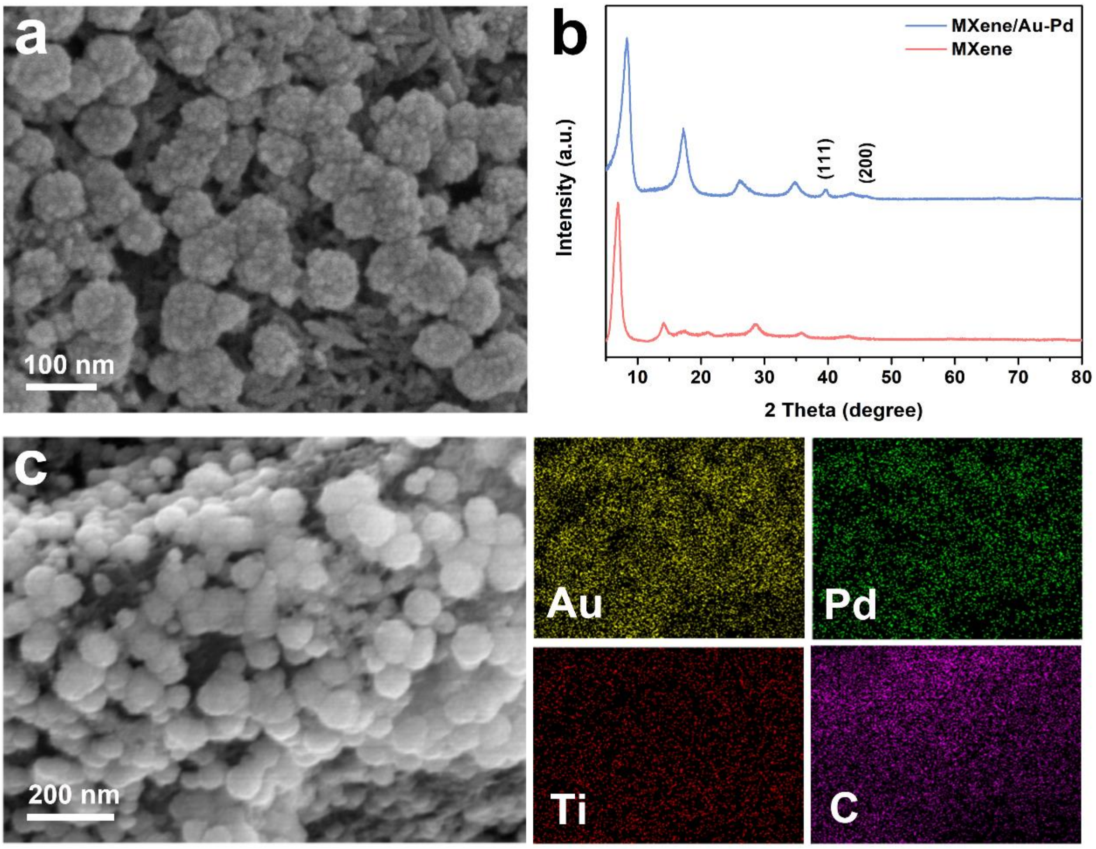
a
100 nm
b
MXene/Au-Pd
MXene
Intensity (a.u.)
(111)
(200)
10
20
30
40
50
60
70
80
2 Theta (degree)
c
200 nm
Au
Pd
Ti
C

Figure 5.

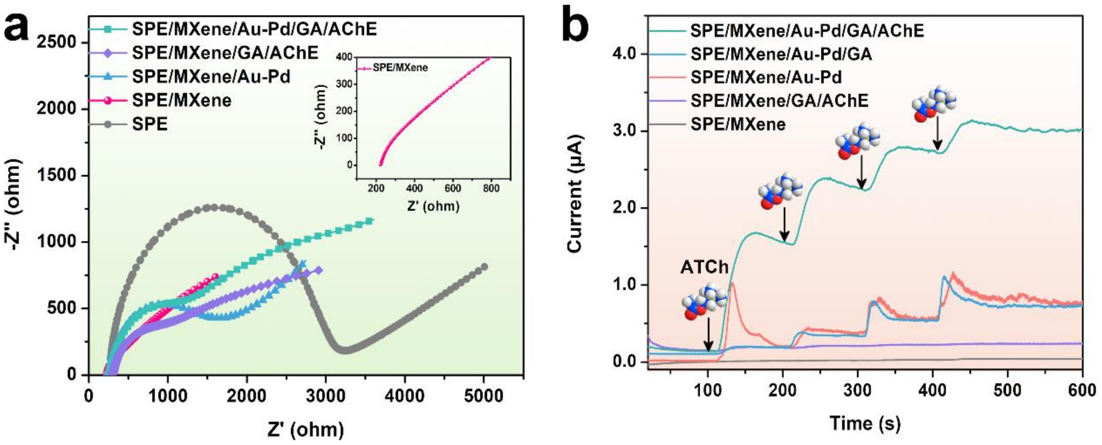
a
SPE/MXene/Au-Pd/GA/AChE
SPE/MXene/GA/AChE
SPE/MXene/Au-Pd
SPE/MXene
SPE
-Z'' (ohm)
Z' (ohm)
0
500
1000
1500
2000
2500
0
1000
2000
3000
4000
5000
SPE/MXene
-Z'' (ohm)
Z' (ohm)
0
100
200
300
400
200
400
600
800
b
SPE/MXene/Au-Pd/GA/AChE
SPE/MXene/Au-Pd/GA
SPE/MXene/Au-Pd
SPE/MXene/GA/AChE
SPE/MXene
ATCh
Current (μA)
Time (s)
0.0
1.0
2.0
3.0
4.0
100
200
300
400
500
600

Figure 6.

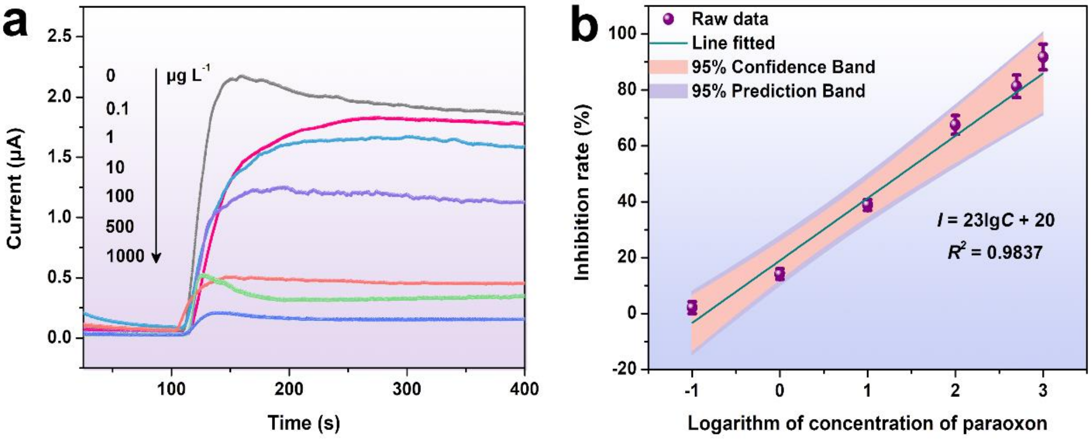
a
Current (μA)
2.5
2.0
1.5
1.0
0.5
0.0
0
0.1
1
10
100
500
1000
μg L^{-1}
100
200
300
400
Time (s)
b
Raw data
Line fitted
95% Confidence Band
95% Prediction Band
Inhibition rate (%)
100
80
60
40
20
0
-20
I = 23lg$C$ + 20
R^2 = 0.9837
-1
0
1
2
3
Logarithm of concentration of paraoxon